Design and experimental verification of advanced control strategies to provide ancillary services with a bidirectional Vehicle-to-Grid (V2G) inverter

Matthias Luh, Thomas Blank
Institute for Data Processing and Electronics (IPE), Karlsruhe Institute of Technology (KIT)
Hermann-von-Helmholtz-Platz 1
76344 Eggenstein-Leopoldshafen, Germany
Tel.: +49 / (0) 721 608-29167
E-Mail: Matthias.Luh@kit.edu, Thomas.Blank@kit.edu
URL: https://www.ipe.kit.edu/english/

Keywords

«AC-DC converter», «Charging infrastructure for EV´s», «Synthetic inertia control», «PLL», «Experimental testing».

Abstract

Vehicle-to-Grid (V2G) may contribute significantly to supporting renewable electricity grids in the future. In addition to flexibly feeding back energy into the grid, V2G inverters could also provide ancillary services to actively stabilize the grid. This paper presents different controller structures for providing ancillary system services with bidirectional AC/DC inverters, such as virtual inertia, frequency, and voltage control. After providing detailed examples of the controllers, we verify them on our prototype and discuss the measurements. The results show that V2G inverters can indeed contribute to grid stabilization.

Introduction

In the course of the energy transition, renewable energy sources (RES) and storage systems are increasingly replacing fossil power plants. Due to the decreasing share of centralized fossil power plants in the electricity grid, it is becoming increasingly important that the (primarily decentral) RES and storage systems take over the ancillary services of conventional power plants, for example (see [1], [2], [3, p. 222]):

- Frequency control (inertia, primary, secondary, tertiary)
- Congestion management & long-term stability (e.g., redispatch, feed-in and demand side management, peak-shaving, valley-filling, interruptible loads, capacity reserves, …)
- Voltage control (reactive power support, voltage imbalance mitigation)
- Fault handling & transient grid stability (e.g., low/high voltage and fault ride through, short-circuit capability, …)
- Black start capability
- Power quality measures (e.g., oscillation damping)

Several ancillary services could also be provided by electric vehicle (EV) charging systems in the future, both by conventional unidirectional chargers and bidirectional Vehicle-to-Grid (V2G) systems. The potential is enormous: For instance, in Germany, although only about 2.2% of passenger cars are battery electric vehicles and 1.8% are plug-in hybrids as of April 2023 [4], their cumulative storage capacity of about 71 GWh [5], [6] already significantly exceeds the storage capacity of pumped storage power plants (39 GWh) and stationary battery storage systems (8 GWh) combined [7], [8]. At the same time, these EVs had a combined DC charging capacity of approximately 100 GW and a combined AC charging capacity of about 12.5 GW [6]. As a comparison, Germany's non-renewable power plant capacity was about 81.6 GW at the end of 2022 [9]. It is evident that only a fraction of the EV battery capacity and charging power can be used in a grid-serving manner. Nevertheless, the order of magnitude indicates that EVs could significantly contribute to grid stabilization.
Most of the ancillary services outlined are characterized by the need to inject or absorb active or reactive power at specific times or under specific conditions and in compliance with specific rules or standards. Therefore, as we will demonstrate in this paper, many of them can not only be realized with conventional rotating generator systems but also with inverters such as those found in V2G chargers. Within certain limits, power electronics with the control

algorithms presented in the following can be used to adjust active and reactive power in a very flexible and dynamic way to fulfill these services – sometimes even better than rotating generators. Several basic ancillary services (such as voltage regulation and, to some extent, frequency regulation) are already mandated for some RES (e.g., in Requirements for Generators (RfG) [10]) and could be similarly required or financially rewarded for V2G chargers.

Experimental Setup

We use the 22 kW three-phase Auxiliary Resonant Commutated Pole Inverter (ARCPI) shown in Fig. 1. It is a bidirectional AC/DC converter based on a voltage-source two-level inverter. In addition to the three half-bridges, auxiliary circuits consisting of additional switches, resonant inductors, and capacitors are used to enable zero-voltage soft switching (Fig. 2). This increases efficiency and allows the use of a higher switching frequency. The principle of operation is explained in more detail in [11].

An FPGA receives PWM settings (one per half-bridge) from a microprocessor and coordinates the soft switching by generating the exact switching patterns for all MOSFETs. The microprocessor calculates the PWM duty cycles based on the desired setpoint current using space vector modulation (SVM). It is also responsible for high-level control algorithms, like voltage control or virtual inertia (VI).

The soft-switching procedure works independently of the control algorithms presented in this paper. Therefore, they can be adapted to other inverter topologies.

We use two similar bidirectional ARCPI inverters connected to separate bidirectional DC power supplies to test the control algorithms easily and comprehensively (see Fig. 3). The first inverter forms an AC grid with adjustable voltage amplitudes and frequency. The half bridges are operated with fixed sinusoidal PWM duty cycle patterns based on the desired frequency – only the voltage amplitude is regulated by modifying the duty cycle intensities. The second inverter is the device under test (DUT), on which the investigated control algorithms are implemented – all measurements were taken close to it.

The advantage of this setup is that arbitrary voltage and frequency profiles can be generated easily and inexpensively, which is not possible on demand in the public electricity grid. The disadvantage compared to commercial Power Hardware-in-the-Loop (PHiL) test systems or the connection to the public grid is that grid impedances and realistic disturbances (such as harmonics, low-frequency oscillations, or grid interferences) cannot be reproduced easily and realistically. Therefore, more extensive testing on PHiL systems and the public power grid is necessary to validate the desired functionality and stability of the controllers and parameters.

For grid services such as VI, widespread implementation also requires critical monitoring of how well frequency stabilization works when many inverters distributed across a large area provide synthetic inertia – something that can hardly be validated in any test environment.

Fig. 1: Photo of the AC/DC converter prototype

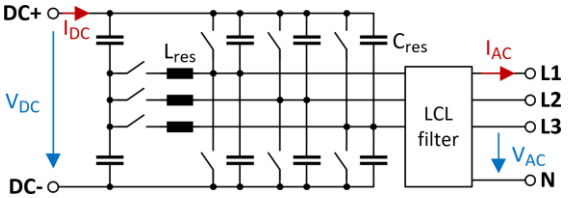

Fig. 2: Simplified schematic of the ARCPI

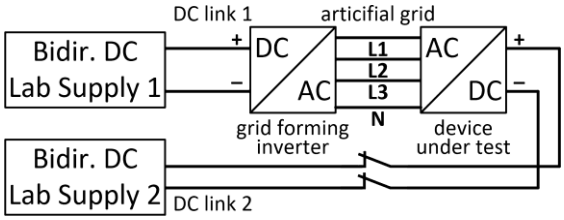

Fig. 3: Test setup: The presented control algorithms are running on the right inverter

Controller structure

The general architecture of the controller is depicted in Fig. 4. It is similar to the structure typically used in grid-tied inverters, comprising a phase-locked loop (PLL) to detect the grid frequency and phase, a current controller, and a PWM algorithm using SVM. However, instead of a regular single reference frame (SRF) PLL, we use a decoupled double synchronous reference frame (DDSRF) PLL (see Fig. 5) that can detect both positive and negative sequence voltages and currents $v/i_{d/q\,+/-}$ [12], [13], [14]. Moreover, several high-level controller algorithms (e.g., DC

link voltage control, AC voltage and frequency control, VI emulation) are implemented to analyze how well some of the mentioned ancillary services can be implemented on a V2G inverter. In addition, a superimposed nominal active and reactive power (symmetric or asymmetric) can be set by the user or an external automated system via CAN or UART. For example, this could be an external controller aggregating similar V2G chargers to trade energy or flexibility on energy markets.

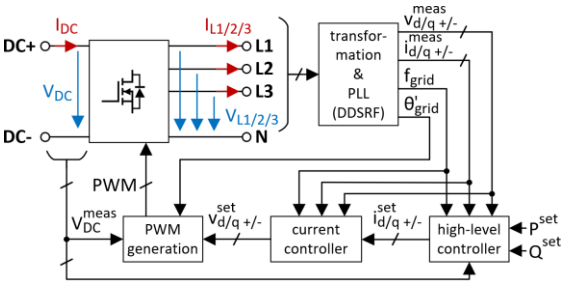

Fig. 4: Top-level structure of the controller

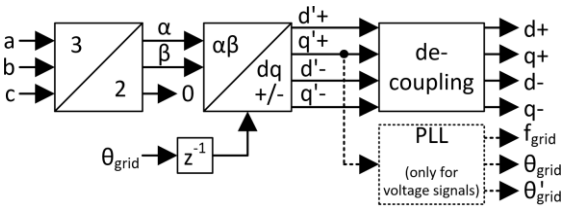

Fig. 5: Voltage/current transformations & PLL

The voltages (and likewise, the currents) are transformed with the well-known amplitude-invariant Clarke-Transformation (1) and a Park-Transformation for both the positive and negative sequence reference frames (2) – rotating in opposite directions without a phase offset.

$$\begin{bmatrix} v_\alpha \\ v_\beta \\ v_0 \end{bmatrix} = \begin{bmatrix} \frac{2}{3} & -\frac{1}{3} & -\frac{1}{3} \\ 0 & \frac{1}{\sqrt{3}} & -\frac{1}{\sqrt{3}} \\ \frac{1}{3} & \frac{1}{3} & \frac{1}{3} \end{bmatrix} \begin{bmatrix} v_a \\ v_b \\ v_c \end{bmatrix} \quad (1)$$

$$\begin{bmatrix} v_{d+} \\ v_{q+} \\ v_{d-} \\ v_{q-} \end{bmatrix} = \begin{bmatrix} \cos\theta & \sin\theta \\ -\sin\theta & \cos\theta \\ \cos\theta & -\sin\theta \\ \sin\theta & \cos\theta \end{bmatrix} \begin{bmatrix} v_\alpha \\ v_\beta \end{bmatrix} \quad (2)$$

The DDSRF-PLL is mostly similar to the structure initially proposed by Rodriguez et al. [12]. However, we use a different filtering method for the current output. Usually, the voltage and current signals are low-pass filtered in the decoupling circuit to significantly attenuate the component of the opposite sequence, which oscillates with twice the grid frequency. However, applying a low-pass filter (LPF) to the $i_{d/q+/-}$ currents introduces a significant delay in the control loop and thus limits the maximum stable speed of the current controller. Revelo et al. [15] use notch filters (NF) instead of LPFs for the current decoupling to only eliminate the frequency component of the opposite sequence – this allows using faster current controllers. We experienced an even better performance/stability trade-off if an LPF is applied to the decoupling circuit, but an NF is used for the current signals passed to the current controllers. Since the performance requirement for the voltage control is much lower, we only use an LPF for the voltages (see Fig. 6).

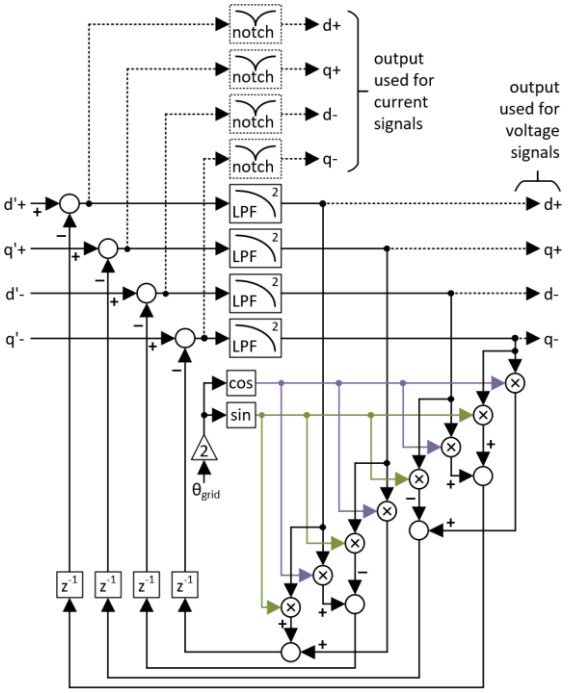

Fig. 6: Decoupling network of our DDSRF-PLL

Both the voltage and current signal LPFs are second-order LPFs using parameters (3)-(7) in the general digital filter transfer function (8).

$$a_0 = 1 + \frac{2}{Q_{LPF} \cdot \omega_{LPF} \cdot T_s} + \left(\frac{2}{\omega_{LPF} \cdot T_s}\right)^2 \quad (3)$$

$$a_1 = 2 \cdot \left(1 - \left(\frac{2}{\omega_{LPF} \cdot T_s}\right)^2\right) \quad (4)$$

$$a_2 = 1 - \frac{2}{Q_{LPF} \cdot \omega_{LPF} \cdot T_s} + \left(\frac{2}{\omega_{LPF} \cdot T_s}\right)^2 \quad (5)$$

$$k_0 = \frac{1}{a_0} \; k_1 = 2k_0 \qquad k_2 = k_0 \quad (6)$$

$$m_0 = 1 \; m_1 = \frac{a_1}{a_0} m_2 = \frac{a_2}{a_0} \quad (7)$$

$$H[z] = \frac{k_0 + k_1 \cdot z^{-1} + k_2 \cdot z^{-2}}{m_0 + m_1 \cdot z^{-1} + m_2 \cdot z^{-2}} \quad (8)$$

We chose $\omega_{LPF} = 2\pi \cdot (0.42 \cdot f_{nom})$ and $Q_{LPF} = 0.35$ with $T_s = 50\ \mu s$ (20 kHz controller/sampling frequency) and $f_{nom} = 50$ Hz (grid frequency).
The current NF uses transfer function (8) with parameters (9)-(14).

$$a_0 = \omega_{notch}^2 + \left(\frac{2}{T_s}\right)^2 \tag{9}$$

$$a_1 = 2\left(\omega_{notch}^2 - \left(\frac{2}{T_s}\right)^2\right) \tag{10}$$

$$b_0 = \left(\omega_{notch}^2 + \frac{\omega_{notch}}{Q_{notch}} \cdot \frac{2}{T_s} + \left(\frac{2}{T_s}\right)^2\right) \tag{11}$$

$$b_2 = \left(\omega_{notch}^2 - \frac{\omega_{notch}}{Q_{notch}} \cdot \frac{2}{T_s} + \left(\frac{2}{T_s}\right)^2\right) \tag{12}$$

$$k_0 = \frac{a_0}{b_0}\ k_1 = \frac{a_1}{b_0}\ k_2 = k_0 \tag{13}$$

$$m_0 = 1\ m_1 = k_1 \qquad m_2 = \frac{b_2}{b_0} \tag{14}$$

We selected $\omega_{notch} = 2\pi \cdot (2 \cdot f_{nom})$, $f_{BW} = 15$ Hz and $Q_{notch} = f_{notch}/f_{BW}$.
The PLL (shown in Fig. 7) estimates the grid frequency and phase by filtering the v_{q+} component using transfer function (8) with parameters (15)-(18) as described in [14].

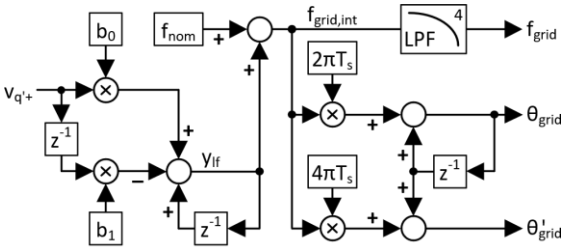

Fig. 7: Phase-locked loop with a frequency filter

$$\omega_n = \frac{\ln\left(1/\left(\delta \cdot \sqrt{1-\zeta^2}\right)\right)}{t_s \cdot \zeta} \tag{15}$$

$$K_p = 2\zeta \frac{\omega_n}{v_{nom}} \qquad K_i = \frac{\omega_n^2}{v_{nom}} \tag{16}$$

$$k_0 = \left(\frac{K_i T_s + 2K_p}{2}\right)\ k_1 = \left(\frac{K_i T_s - 2K_p}{2}\right) \tag{17}$$

$$m_0 = 1\ m_1 = -1 \qquad m_2 = k_2 = 0 \tag{18}$$

We selected the error band $\delta = 0.1$, the damping ratio $\zeta \approx 0.247$, the settling time $t_s \approx 0.168$, and used $v_{nom} = 230 \cdot \sqrt{2}$. This results in $\omega_n \approx 56.1$, $K_p \approx 0.0854$, and $K_i \approx 9.6765$.
The filter outputs $f_{grid,int}$, and the grid phase θ_{grid} is incremented by $2\pi \cdot T_s \cdot f_{grid,int}$ in each step.
The controller is pipelined: The FPGA acquires measurements in control cycle i, the current controller in the microprocessor is active in cycle i+1, and the FPGA applies the PWM in cycle i+2. To compensate for this delay, an additional phase increment is added to the grid phase to obtain θ'_{grid}, which is used for the back transformation in the microprocessor.
The PLL filters the internal grid frequency with a fourth-order LPF to generate a much smoother signal that can be used in the frequency control algorithms. A relatively slow LPF is used with a fourth-order transfer function in the form of (8) using $\omega_1 = 2\pi \cdot 8$ Hz, $\omega_2 = 2\pi \cdot 4$ Hz, $Q_1 = 0.45$, $Q_2 = 0.35$, and the parameters:

$$a = 1/(Q_1 \cdot \omega_1)\ b = 1/\omega_1^2 \tag{19}$$

$$c = 1/(Q_2 \cdot \omega_2)\ d = 1/\omega_2^2 \tag{20}$$

$$e = (a + c) \cdot (2/T_s) \tag{21}$$

$$f = (ac + b + d) \cdot (2/T_s)^2 \tag{22}$$

$$g = (bc + ad) \cdot (2/T_s)^3 \tag{23}$$

$$h = bd \cdot (2/T_s)^4 \tag{24}$$

$$\begin{bmatrix} a_0 \\ a_1 \\ a_2 \\ a_3 \\ a_4 \end{bmatrix} = \begin{bmatrix} 1 & 1 & 1 & 1 & 1 \\ 4 & 2 & 0 & -2 & -4 \\ 6 & 0 & -2 & 0 & 6 \\ 4 & -2 & 0 & 2 & -4 \\ 1 & -1 & 1 & -1 & 1 \end{bmatrix} \begin{bmatrix} 1 \\ e \\ f \\ g \\ h \end{bmatrix} \tag{25}$$

$$\begin{bmatrix} k_0 \\ k_1 \\ k_2 \\ k_3 \\ k_4 \end{bmatrix} = \begin{bmatrix} 1 \\ 4 \\ 6 \\ 4 \\ 1 \end{bmatrix} \cdot \frac{1}{a_0} \quad \begin{bmatrix} m_0 \\ m_1 \\ m_2 \\ m_3 \\ m_4 \end{bmatrix} = \begin{bmatrix} a_0 \\ a_1 \\ a_2 \\ a_3 \\ a_4 \end{bmatrix} \cdot \frac{1}{a_0} \tag{26}$$

The structure of the current controller is shown in Fig. 8. It is comparable to an SRF current controller but extended by the negative sequence currents. The signs of decoupling terms (crossing signals on the right side) depend on the direction of the reference frame rotation and the current measurement (defined in Fig. 4). By injecting negative sequence currents, continuous or transient voltage asymmetries in the distribution grid can be compensated. Different methods are analyzed and compared in [15].
The voltage setpoints are transformed back to the stationary reference form with the inverse Park- and Clarke-Transformations (27)-(29), adjusted to the dual reference frames. After the transformations, the PWM duty cycles are calculated based on $v_{a/b/c}$ and V_{DC}.

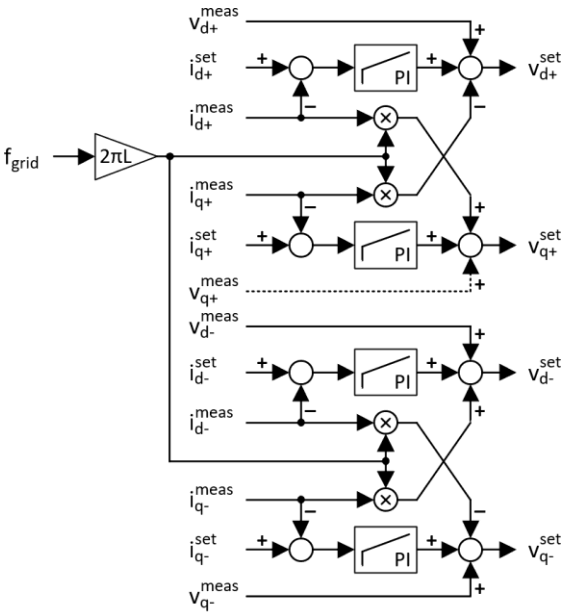

Fig. 8: DDSRF current controller

$$v_\alpha = v_{d+} \cdot \cos\theta - v_{q+} \cdot \sin\theta + v_{d-} \cdot \cos\theta + v_{q-} \cdot \sin\theta \quad (27)$$

$$v_\beta = v_{d+} \cdot \sin\theta + v_{q+} \cdot \cos\theta - v_{d-} \cdot \sin\theta + v_{q-} \cdot \cos\theta \quad (28)$$

$$\begin{bmatrix} v_a \\ v_b \\ v_c \end{bmatrix} = \begin{bmatrix} 1 & 0 & 1 \\ -\frac{1}{2} & \frac{\sqrt{3}}{2} & 1 \\ -\frac{1}{2} & -\frac{\sqrt{3}}{2} & 1 \end{bmatrix} \begin{bmatrix} v_\alpha \\ v_\beta \\ v_0 \end{bmatrix} \quad (29)$$

In its basic form, the high-level controller only includes a DC link voltage controller (see Fig. 9), which adjusts the AC active power in addition to P^{set} and Q^{set} to hold the DC link voltage at the desired level.

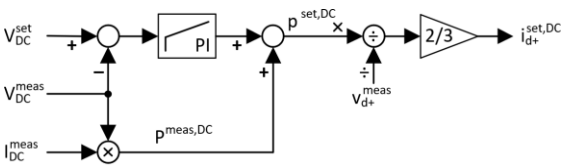

Fig. 9: DC link voltage controller

Moreover, a frequency and voltage controller can be enabled and dynamically adjusted during operation. The frequency control includes a virtual inertia algorithm. Tamrakar et al. [16] give an overview of such VI topologies. We have analyzed different Synchronverters and a Virtual Synchronous Generator (VSG) in preceding simulations. The VSG was by far the easiest topology to implement and tune, and it operated very stably. Therefore, we implemented this topology on our prototype (see Fig. 10). It includes a term for frequency containment reserve (FCR), which reacts to a deviation Δf. The second term reacts to a frequency change d/dt(Δf). It provides synthetic inertia by injecting an additional current i_{d+} to adjust active power feed-in or demand based on the direction and magnitude of the frequency change.

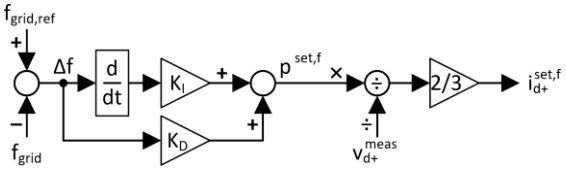

Fig. 10: Frequency control and VI with a VSG

We picked K_I = 1 kW/(Hz/s) and K_D = 2.5 kW/Hz. In practice, the derivation term needs to be carefully designed: Measurement noise, quantization errors, and the interaction with the PLL in combination with the often relatively slow frequency changes (typically in the range of a few mHz/s, even during severe incidents seldomly above 1 Hz/s) make it difficult to calculate a smooth output power accurately. Therefore, the derivation term does not simply calculate the difference of successive values. Instead, the controller uses a derivation term that utilizes a 200 ms long ring buffer filled with frequency values averaged from 32 control cycles. Below an adjustable limit of currently 2 mHz/s, the VI output component is set to 0 to avoid permanent activity on the V2G charger and the EV battery.

The AC voltage controller, in its simple form, only reacts to the positive sequence voltage v_{d+} (see Fig. 11). A current i_{q+}, i.e., reactive power, is injected based on the deviation from the nominal voltage v_d^{nom} and a given profile (typically specified in the RfG, e.g., see [17, Fig. 1.3]).

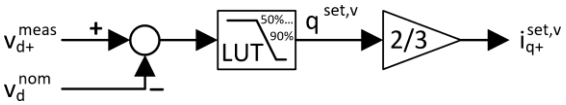

Fig. 11: AC voltage control providing reactive power based on predefined look-up tables

Experimental results and discussion

In the following, we analyze the results we collected using the previously described hardware and different parts of the controller. The grid-forming inverter (see Fig. 3) always operates with a fixed AC voltage of 110 V_{RMS} and a fixed frequency of 50 Hz unless otherwise stated.

At first, all high-level controllers are disabled. A setpoint step from a symmetrical power P_{set} = -3.5 kW (load) to +3.5 kW (generation) is applied (see Fig. 12a). Fig. 12b shows another

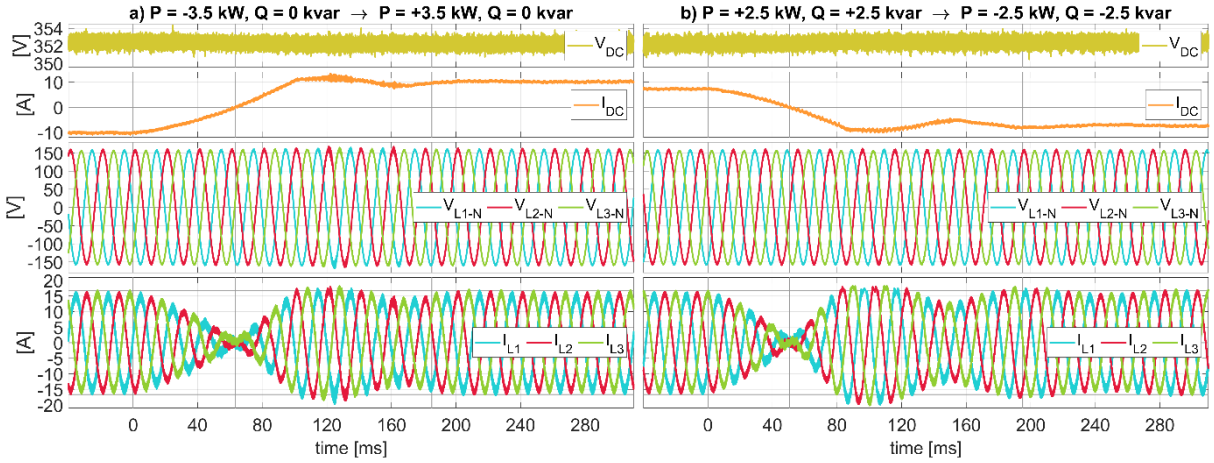

Fig. 12: Setpoint step changes with symmetrical power: a) from -3.5 kW (load) to +3.5 kW (gen.), b) from +2.5 kW (gen.), +2.5 kvar (cap. gen./ind. load.) to -2.5 kW (load), -2.5 kvar (cap. load/ind. gen.) From top to bottom: DC link voltage (yellow) and current (orange), AC voltages, AC currents.

setpoint step with a reactive power component. In both cases, the controlled variable reaches the new setpoint and settles within 200 ms.

The currents $i_{d/q\,+/-}$ can also be specified individually, allowing asymmetric power levels. In the first period of Fig. 13, I_{L3} is eliminated. Since the inverter can only control the three phases but not the neutral current (this would require a fourth half-bridge), no zero sequence currents can be injected, so in vectorial representation, $I_{L1} + I_{L2} + I_{L3} = 0$. In other words, without rewiring, it is impossible to arbitrarily set two phase currents, e.g., to enable a single-phase operation or a two-phase operation with solely active power. Instead, in the first period of Fig. 13, the resulting reactive power is distributed evenly to the phases. In the second period, I_{L2} is eliminated and the reactive power of the first phase is reduced. The current of the third phase results in $I_{L3} = -I_{L1}$. After the setpoint step, the new setting is reached and settled in about 100 ms.

Next, the grid-forming inverter generates a low-voltage fault event, during which it quickly reduces the AC voltage from 110 V to 50 V. The AC voltage controller of the other inverter (DUT) provides reactive power during the voltage sag, as shown in Fig. 14 and Fig. 15. Since no active power is needed, this is even possible if the DC link of the DUT is open (e.g., a stationary DC charger to which no EV is connected). Only the power losses and the transients in the DC link (particularly visible in Fig. 14b) need to be compensated, so the DC voltage controller must also be active. When activated from standby with discharged DC link, the inverter is ready to provide power within one second, including the precharge phase. When energized, the inverter

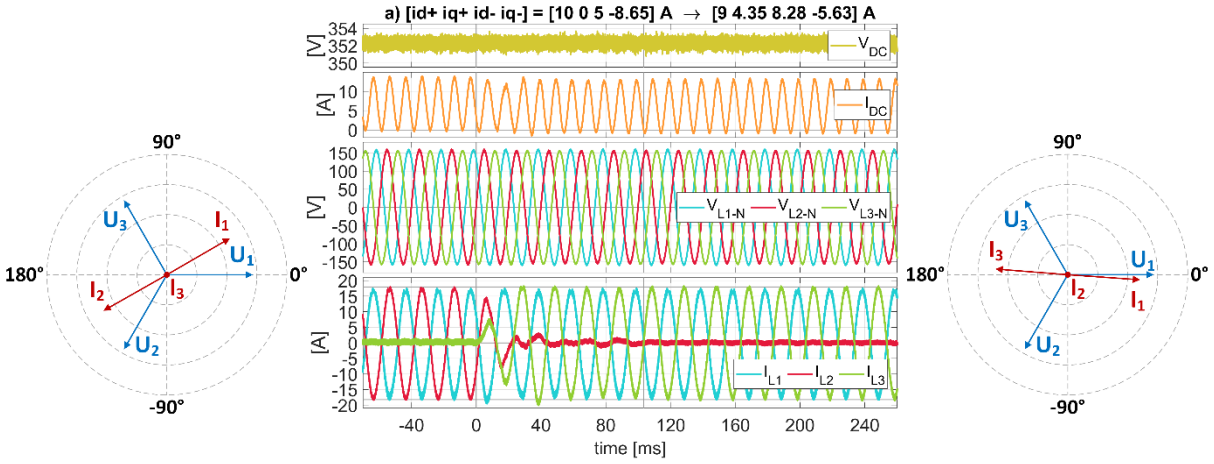

Fig. 13: Asymmetric current setpoint change: From $i_{d+} = 10$ A, $i_{q+} = 0$ A, $i_{d-} = 5$ A, $i_{q-} = -8.65$ A (elimination of I_{L3}, see left vector diagram) to $i_{d+} = 9$ A, $i_{q+} = 4.35$ A, $i_{d-} = 8.28$ A, $i_{q-} = -5.63$ A (elimination of I_{L2}, reactive power on phase 1 minimized, see right vector diagram)

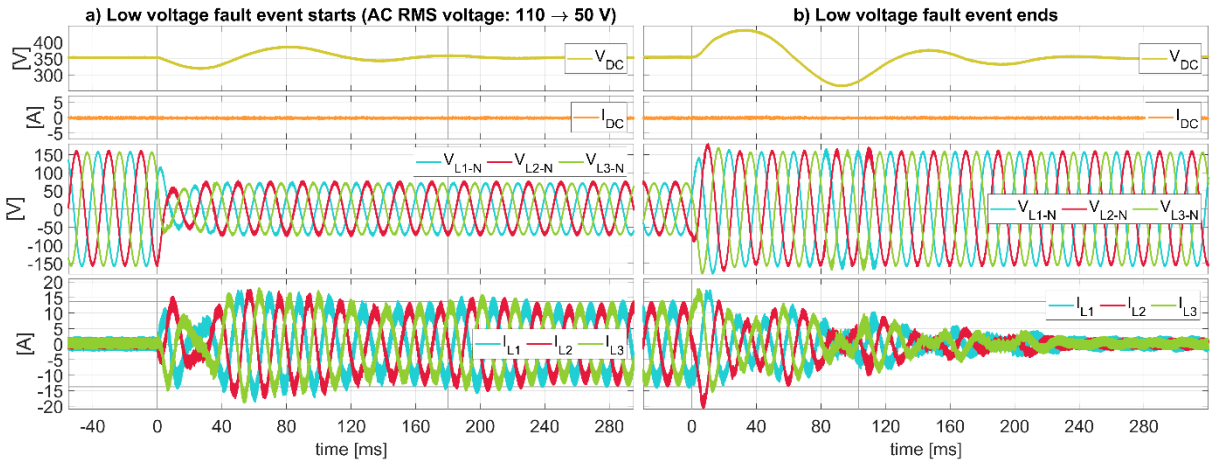

Fig. 14: Low-voltage ride through (LVRT) – AC voltage control with open/unconnected DC link: a) fault event start ($V_{AC,RMS}$ drops from 110 V to 50 V, inverter feeds in inductive reactive power) b) fault end ($V_{AC,RMS}$ recovers, reactive power is reduced, disturbance in the DC link is compensated)

provides reactive power within approximately 40 ms and settles in about 200 ms after the beginning of the voltage sag (as shown in Fig. 14). After the voltage rises again, the controller's overcurrent protection limits the current increase during the first 10-20 ms. Meanwhile, the AC voltage controller reduces reactive power and the DC voltage controller adjusts the DC voltage within ca. 250 ms.

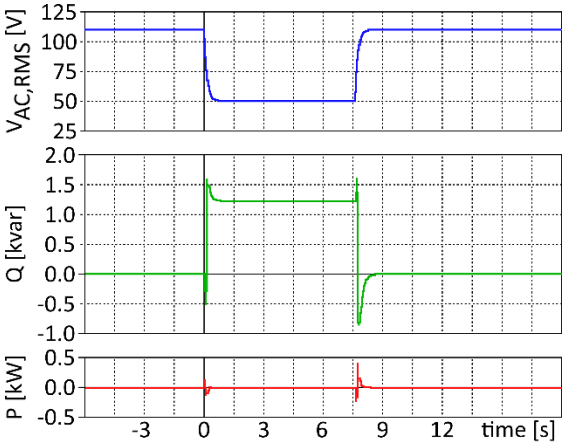

Fig. 15: Voltage sag (blue) and reactive (green) and active (red) power as in Fig. 14, recorded with a Hioki PW3390

Finally, the frequency control (FC) and virtual inertia (VI) algorithm is tested. For this purpose, we extracted the frequency drop of the system split in the Continental Europe Synchronous Area on 24 July 2021 at the Hernani substation from [18, pp. 96–97]. We modified the data after the minimum frequency is reached (5 s after the beginning of the event) so the frequency returns to the initial frequency of approximately 49.96 Hz quickly.

The grid-forming inverter follows the frequency profile and the DUT shall vary active power either based on the frequency deviation Δf to 50 Hz (FC), the frequency change d/dt(Δf) (VI), or both. An active power setpoint of P_{set} = -1 kW was selected before the frequency event to emulate EV charging. The FC response to the frequency deviation is clearly visible in Fig. 16a. It follows the frequency profile with a delay of about 150 ms, which is due to the PLL and the frequency low-pass filter.

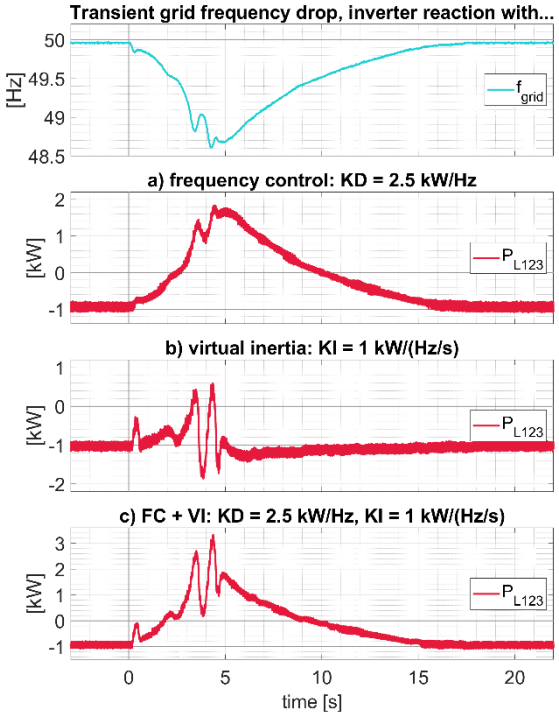

Fig. 16: Frequency control and virtual inertia reaction to a grid frequency drop. P_{set} = -1 kW.

The response of the VI controller in Fig. 16b can also be recognized. Due to the filtered differentiator, the delay of 200 ms to the frequency curve is slightly higher. In Fig. 16c, both the FC and VI terms are active.
If a significantly higher parameter K_I is chosen (or a considerably faster differentiator filter is used), unstable behavior may occur after drastic frequency changes (such as in the analyzed case) since large changes in the feed-in power lead to small but noticeable disturbances in the PLL output, which in turn affects the VI power. On the other hand, the effect of the VI algorithm is hardly recognizable when using a very small parameter K_I. As a possible improvement, a higher-order low-pass filter with a suitably low cutoff frequency could be implemented for the grid frequency so that a considerable reaction is evoked for the frequency changes in the range of 0-3 s as well as 5-18 s in Fig. 16, but disturbances such as in the range around 4 s (which could also be caused by switching procedures in substations) do not trigger an unstable behavior.
Although the presented VI algorithm controls active power based on the frequency deviation and derivation, the inverter does not actively change the grid frequency but only follows it. That means that this simple type of VI cannot replace conventional inertia or grid-forming inverters that can restore the nominal frequency, but it can only support them.

Conclusion

We presented the control structure of a bidirectional three-phase grid-tied inverter to be used in a Vehicle-to-Grid charger. It has a high degree of flexibility and contains advanced grid control features to provide ancillary services, which we explained in detail. We illustrated the structure of a DDSRF-PLL, which can inject arbitrary positive and negative sequence currents relatively quickly and assures stable operation even under asymmetric grid conditions. Furthermore, we presented a frequency controller, which can provide synthetic inertia to stabilize the grid frequency. We then verified and discussed the various controllers (symmetrical active/reactive power, asymmetrical currents, DC link and AC line voltage, frequency, and virtual inertia control) on our prototype. The results indicate that our V2G inverter can not only feed back power into the electricity grid but actively contribute to its stabilization. However, the higher complexity and additional energy required to provide these ancillary services would have to be either required by regulation or financially rewarded for widespread adoption.

References

[1] Kaushal A. and Van Hertem D.: An Overview of Ancillary Services and HVDC Systems in European Context, Energies, vol. 12, no. 18, p. 3481, 2019, DOI 10.3390/en12183481

[2] Sevdari K., Calearo L., Andersen P.B., et al.: Ancillary services and electric vehicles: An overview from charging clusters and chargers technology perspectives, Renewable and Sustainable Energy Reviews, vol. 167, p. 112666, 2022, DOI 10.1016/j.rser.2022.112666

[3] Monitoringbericht 2022, Bundesnetzagentur für Elektrizität, Gas, Telekommunikation, Post und Eisenbahnen; Bundeskartellamt, Bonn, Germany, 2022

[4] Kraftfahrt-Bundesamt: Vierteljährlicher Bestand, Apr-2023. [Online]. Available: https://www.kba.de/DE/Statistik/Fahrzeuge/Bestand/Vierteljaehrlicher_Bestand/viertelj%C3%A4hrlicher_bestand_node.html. [Accessed: 20-Jun-2023]

[5] Christopher Hecht, Jan Figgener, and Dirk Uwe Sauer: Mobility Charts, Mobility Charts, Apr-2023. [Online]. Available: https://www.mobility-charts.de/. [Accessed: 20-Jun-2023]

[6] Hecht C., Spreuer K.G., Figgener J., et al.: Market Review and Technical Properties of Electric Vehicles in Germany, Vehicles, vol. 4, no. 4, pp. 903–916, 2022, DOI 10.3390/vehicles4040049

[7] Figgener J., Hecht C., Haberschusz D., et al.: The development of battery storage systems in Germany: A market review (status 2022). 15-Mar-2022, DOI 10.48550/arXiv.2203.06762

[8] Fraunhofer ISE: Net installed electricity generation capacity in Germany in 2023, energy-charts.info, 2023. [Online]. Available: https://energy-charts.info/charts/installed_power/chart.htm?l=en&c=DE&year=2023&chartColumnSorting=default&legendItems=000001&interval=month. [Accessed: 20-Jun-2023]

[9] Burger B.: Öffentliche Nettostromerzeugung in Deutschland im Jahr 2022, Freiburg, 01-Oct-2023

[10] Commission Regulation (EU) 2016/631 of 14 April 2016 establishing a network code on requirements for grid connection of generators, 2016

[11] Luh M. and Blank T.: Auxiliary Resonant Commutated Pole Inverter (ARCPI) with SiC MOSFETs for efficient Vehicle-to-Grid (V2G)

charging, in 2021 23rd European Conference on Power Electronics and Applications (EPE'21 ECCE Europe), 2021, DOI 10.23919/EPE21ECCEEurope50061.2021.9570620

[12] Rodriguez P., Pou J., Bergas J., et al.: Decoupled Double Synchronous Reference Frame PLL for Power Converters Control, IEEE Transactions on Power Electronics, vol. 22, no. 2, pp. 584–592, 2007, DOI 10.1109/TPEL.2006.890000

[13] Graungaard Taul M., Wang X., Davari P., et al.: Current Reference Generation Based on Next-Generation Grid Code Requirements of Grid-Tied Converters During Asymmetrical Faults, IEEE Journal of Emerging and Selected Topics in Power Electronics, vol. 8, no. 4, pp. 3784–3797, 2020, DOI 10.1109/JESTPE.2019.2931726

[14] Bhardwaj M.: Software Phase Locked Loop Design Using C2000™ Microcontrollers for Three Phase Grid Connected Applications, Texas Instruments, 2013

[15] Revelo S. and Silva C.A.: Current reference strategy with explicit negative sequence component for voltage equalization contribution during asymmetric fault ride through: Current Strategy with Negative Sequence Component, Int. Trans. Electr. Energ. Syst., vol. 25, no. 12, pp. 3449–3471, 2015, DOI 10.1002/etep.2045

[16] Tamrakar U., Shrestha D., Maharjan M., et al.: Virtual Inertia: Current Trends and Future Directions, Applied Sciences, vol. 7, no. 7, p. 654, 2017, DOI 10.3390/app7070654

[17] da Silva, R. M.: Power control strategies for grid-connected converters during low voltage ride through operation, Master Thesis, Universidade Federal de Minas Gerais (UFMG) - Escola de Engenharia, 2019

[18] M. Dierick, T. Kapetanovic, A. Marques, et al.: Continental Europe Synchronous Area Separation on 24 July 2021 (ICS Investigation Expert Panel » Final Report » 25 March 2022 - Main Report), The Expert Panel on the separation of the Continental Europe Synchronous Area of 24 July 2021, 2022